ADVANCED MATERIALS INTERFACES

www.advmatinterfaces.de

Check for updates

Solution-Processed Transparent Sn^{4+}-Doped CuI Hybrid Photodetectors with Enhanced Performances

*Siyuan Li, Yong Zhang, Wei Yang, and Xiaosheng Fang**

Herein, Sn^{4+}-doped copper (I) iodide (CuI) is prepared via a facile, cost-efficient solution process, and the properties of Sn^{4+}-doped CuI, including morphology, crystalline phase, as well as optical and electrical properties, are investigated by varying the Sn^{4+} concentration. And by constructing transparent Sn^{4+}-CuI/ZnO hybrid UV photodetectors, the potential of Sn^{4+}-CuI as a p-type material for high-performance photodetection is investigated. It is found that Sn^{4+} doping has great effect on the morphology as the formation of Sn^{4+}-CuI thin sheets is observed, and the resistivity of Sn^{4+}-CuI could be tuned by controlling Sn^{4+} addition. The Sn^{4+}-CuI/ZnO hybrid photodetectors exhibit obviously enhanced photodetecting performance outperforming ZnO film and CuI/ZnO photodetectors by the same preparation method, including significantly improved on/off ratio, spectral responsivity, and shortened responsive time. The enhanced performance of Sn^{4+}-CuI/ZnO hybrid photodetectors mainly arises from the formation of type-II p-Sn^{4+}-CuI/n-ZnO heterojunctions, and the better interface contact leads to higher carrier separation efficiency due to the existence of Sn^{4+}-CuI thin sheets. And the improved performance is also related to the optimized resistivity of Sn^{4+}-CuI. This study sheds light on the potential of doped CuI toward transparent, high-performance photodetectors in the future.

1. Introduction

The world we live in is inundated with electromagnetic waves, and the full-band detection of electromagnetic wave has provided us with an insightful understanding of nature and promoted technological progress. Among them the detection of ultraviolet (UV) radiation with energy higher than that of visible light is of great interest as UV detection has found diverse applications such as environment monitoring, spectral analysis, flame warning, and personal health management.[1–6] In the category of photodetectors, the p–n and p–i–n photodiodes are capable of separating and transporting photoinduced carrier pairs efficiently by built-in electric field, leading to low dark current, rapid response speed, and even operation without external power supply.[7–9] Consequently the fabrication of high-quality photodiodes demands the development of satisfactory p-type semiconductors. Nowadays, much efforts are being made in search of advanced p-type materials with unique properties, such as amorphous, flexible, transparent, and highly conductive p-type semiconductors.[10–12]

Cuprous iodide (CuI) has three main crystalline phases, α, β, and γ, among which γ-CuI with zinc-blende cubic structure exists as the stable phase under temperature of 350 °C. And γ-CuI, a p-type I–VII semiconductor with a direct bandgap of ≈3.1 eV, exhibits many advantages such as transparency, nontoxicity, high conductivity, and high exciton binding energy.[13,14] Up to now, CuI has been effectively utilized in versatile applications such as light-emitting diodes (LEDs), electronics, and catalysis.[15–17] As CuI has high hole conductivity and a valance band maximum aligning well with some solar absorber layers such as perovskite $MAPbI_3$ and so on, nowadays CuI is widely used as an inexpensive dopant or a promising alternative for organic hole transporting materials (such as spiro-OMeTAD) in solar cells, leading to enhanced efficiency and satisfactory stability.[18–20] By far many techniques have been developed and commonly employed for the fabrication of CuI with various size and morphologies, including iodization of copper film, chemical and electrochemical method, sputtering as well as solution process, on various substrates.[13,21–24] Among those, the solution process boasts various advantages such as low cost, facile, easy scale-up, and easiness of doping or forming composites. Yet, CuI is far from being fully exploited as a p-type semiconductor. It has been reported that for CuI, the native p-type conductivity arises mainly from the introduction of intrinsic defect Cu^+ vacancy.[25] Although defect engineering and doping are crucial for manipulating the properties of semiconductors, research reports on doped CuI are still rare. For instance, the electrical and luminescence properties of Zn^{2+}-doped CuI and properties of Li^+-doped CuI were investigated separately while more possible dopants, like Ga and Al, still remain theoretical.[26–28] And CuI film doped with excessive anions, such as iodine and thiocyanate, was also reported.[29] Recently, p-type transparent amorphous Cu-Sn-I film was

S. Y. Li, Dr. Y. Zhang, W. Yang, Prof. X. S. Fang
Department of Materials Science
Fudan University
Shanghai 200433, P. R. China
E-mail: xshfang@fudan.edu.cn

The ORCID identification number(s) for the author(s) of this article can be found under https://doi.org/10.1002/admi.201900669.

DOI: 10.1002/admi.201900669

 © 2019 WILEY-VCH Verlag GmbH & Co. KGaA, Weinheim

prepared by spin-coating of 2-methoxyethanol solution of CuI and annealing in Ar atmosphere, and the addition of Sn^{4+} acts as an inhibitor of fast crystallization and a stabilizer of CuI structure.[12] However, further study on doped CuI is still required toward improved properties and possible applications.

On the other hand, there are a number of promising candidates for ultraviolet photodetectors in the category of n-type wide-bandgap semiconductors, among which ZnO stands out for its remarkable physical and chemical properties, such as suitable bandgap (≈3.37 eV at room temperature) corresponding to the UV region, high carrier mobility, nontoxicity, and low cost.[30,31] To date, ZnO has received in-depth research and many synthetic methods have been explored to fabricate ZnO structures with a rich variety of morphologies, in order to meet the needs of various practical applications.[32,33] However, photodetectors based on ZnO film exhibit some inherent limitations such as slow response to UV light illumination because of O_2 adsorption and desorption process on ZnO surface.[34] The process is particularly obvious in nanocrystalline ZnO due to large specific surface area it exhibits, which impedes its application as a high-performance photodetector. Hence, much efforts have been made to improve the performance of ZnO-based photodetectors, and common approaches include doping, surface modification, and forming heterojunctions.[35–38] In those methods, the fabrication of p–n junctions has been proven as an effective way to facilitate the charge separation and transportation process and decrease O_2 adsorption.[35,37] As a p-type semiconductor with satisfactory properties, CuI has been utilized to fabricate p–n junctions with n-type semiconductors including ZnO, opening possibilities for constructing high-performance photodiodes.[22,39–41] For instance, ZnO-CuI/CuSCN heterojunctions were fabricated by Yang et al. using spin-coating method for UV photodetectors with semitransparency and enhanced performance.[42] And stress-responsive Cu wire/CuI/ZnO photodetectors were fabricated, exhibiting high photocurrent and responsivity.[43] However, many previous fabrication methods of CuI/ZnO heterojunctions require complex procedure and toxic iodine vapor. In addition, the potential of doped CuI toward enhanced photodetecting performance of ZnO film by forming p–n junctions has not been investigated yet.

In this work, Sn^{4+}-doped CuI samples are prepared by simple, low-cost spin-coating technique, and for the first time transparent Sn^{4+}-CuI/ZnO hybrid photodetectors are successfully fabricated for UV photodetection. Herein, the effect of Sn^{4+} doping on copper iodide, including morphology as well as optical and electrical properties, is investigated by varying Sn^{4+} doping concentration utilizing multiple characterization techniques. The Sn^{4+}-CuI/ZnO hybrid photodetectors show obviously improved on/off ratio, responsivity upon UV illumination, and shortened responsive time upon UV light switching, outperforming ZnO film as well as CuI/ZnO photodetectors. The enhanced photodetecting performance of Sn^{4+}-CuI/ZnO hybrid photodetectors mainly results from type-II heterojunction, adjustable resistivity of Sn^{4+}-CuI and the better contact and carrier separation of ultrathin Sn^{4+}-CuI interface. This study sheds light on the potential of doped CuI toward transparent, high-performance photodetectors in the future.

2. Results and Discussion

The Sn^{4+}-CuI samples are prepared by spin-coating acetonitrile/2-methoxyethanol mixed solution containing various molar ratio of CuI and SnI_4, with the picture of solution shown in Figure S1 in the Supporting Information. The size, morphology, and structure of the prepared Sn^{4+}-CuI samples are characterized by scanning electron microscopy (SEM), transmission electron microscopy (TEM), and atomic force microscopy (AFM) methods. **Figure 1** shows the SEM images of obtained Sn^{4+}-doped CuI spin-coated on ZnO nanoparticle film, and the AFM images of spin-coated Sn^{4+}-CuI samples on silicon substrate are shown in Figure S2 in the Supporting Information. The prepared ZnO film is composed of densely packed nanoparticles with average diameter of 30 nm and the thickness of ZnO nanoparticle film is measured as ≈120 nm according to the cross-sectional SEM image. As is seen in Figure 1b, the spin-coated CuI sample is characterized by CuI nanoparticles with average diameter of 50 nm. When 0.5% SnI_4 is added into the CuI solution, the most striking feature of the samples is the formation of Sn^{4+}-CuI sheets. And from AFM height profiles (Figure S2a,b, Supporting Information) the CuI and 0.5% Sn^{4+}-CuI samples are composed of micron-scale agglomerates with height of around 200 and 100 nm, separately, and the decrease in average height of agglomerates would lead to better structural uniformity and better contact with n-type materials in the case of fabrication of heterojunctions. With the Sn^{4+} addition amount increasing to 1%, the Sn^{4+}-CuI sheets exhibit an increase in lateral size (Figure 1d), and it is especially interesting to note that the existence of Sn^{4+}-CuI nanosheets with lateral scale around 2 μm and thickness of ≈11 nm is confirmed by AFM height profile (Figure S2c, Supporting Information). The TEM image in Figure 1g shows the 1% Sn^{4+}-CuI sample is an assembly of nanosize grains. And with an even higher Sn^{4+} addition, however, the Sn^{4+}-CuI sheets tend to stack (Figure 1e) and for 10% Sn^{4+}-CuI protruding sheets with warp distortion are observed (Figure 1f). Furthermore, in Figure S3a in the Supporting Information, the average particle or sheet size estimated by SEM shows that with the increase of Sn^{4+} addition the average particle size of Sn^{4+}-CuI increases dramatically, from 50 nm for CuI to ≈370 nm for 10% Sn^{4+}-CuI samples. At the same time, the particle size deviation rises up with the increasing average particle size, indicating the declined crystalline uniformity with high Sn^{4+} addition. In brief, the results above suggest the feasibility of manipulating the size and morphology of CuI with various Sn^{4+} additions and an optimal concentration of Sn^{4+} is acquired in order to obtain better CuI crystallization.

To determine the phase of Sn^{4+}-CuI samples, high-resolution transmission electron microscopy (HRTEM) and selected area electron diffractions (SAED) are performed, as is shown in Figure 1g,h. The HRTEM images illustrate the interplanar spacing of 0.34 nm for 1% Sn^{4+}-CuI samples, corresponding to the spacing of CuI (111) plane. And the result shows the Sn^{4+} doping has limited influence on the interplanar spacing of CuI lattice as Sn^{4+} shares a similar ion radius with Cu^{+}.[44] In 1% Sn^{4+}-CuI sample, the SAED patterns (Figure 1h) show a mixture of diffraction spots and rings, indicating the polycrystalline

© 2019 WILEY-VCH Verlag GmbH & Co. KGaA, Weinheim

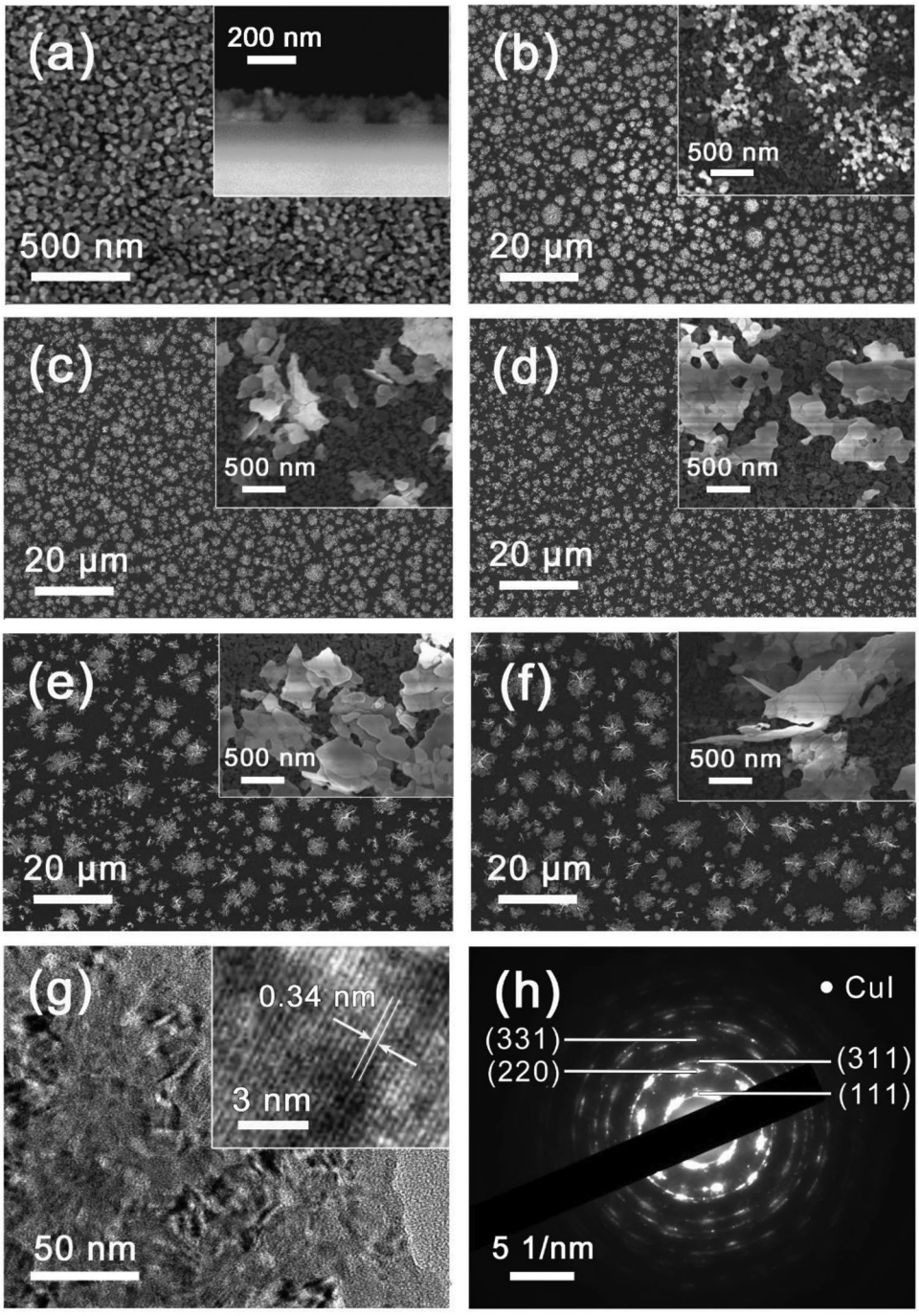

Figure 1. SEM images of a) prepared ZnO nanoparticle film, b) CuI, and Sn^{4+}-doped CuI with c) 0.5%, d) 1%, e) 5%, and f) 10% Sn^{4+} addition by spin-coating method on ZnO film. The insets show cross-sectional SEM image of ZnO film and SEM images at higher magnification. g) TEM image (the inset shows HRTEM image) and h) SAED pattern of 1% Sn^{4+}-CuI.

nature with relatively large crystal size of prepared Sn^{4+}-CuI. The diffraction patterns of (111), (220), (311), and (331) planes of CuI could be clearly observed. And the diffraction patterns from SnI_4 phase are barely discernible, suggesting the successful doping of Sn^{4+} into CuI lattice. In addition, with higher Sn^{4+} addition to 10%, the SnI_4 phase is observed by HRTEM and SAED in Figure S4 in the Supporting Information, indicating the formation of a composite composed of CuI and SnI_4 crystal phases, and the distortion existing in 10% Sn^{4+}-CuI structure is possibly attributed to the lattice mismatch.

To further determine the crystal phase of Sn^{4+}-CuI, the grazing incidence X-ray diffraction (GIXRD) measurement is conducted for pure CuI and Sn^{4+}-CuI samples containing 0.5%, 1%, 5%, and 10% Sn^{4+}, separately. As is shown in **Figure 2**, for CuI and Sn^{4+}-CuI samples, the obtained XRD peaks at 25.5°, 42.2°, 49.9°, and 67.4° match well with the (111), (220),

© 2019 WILEY-VCH Verlag GmbH & Co. KGaA, Weinheim

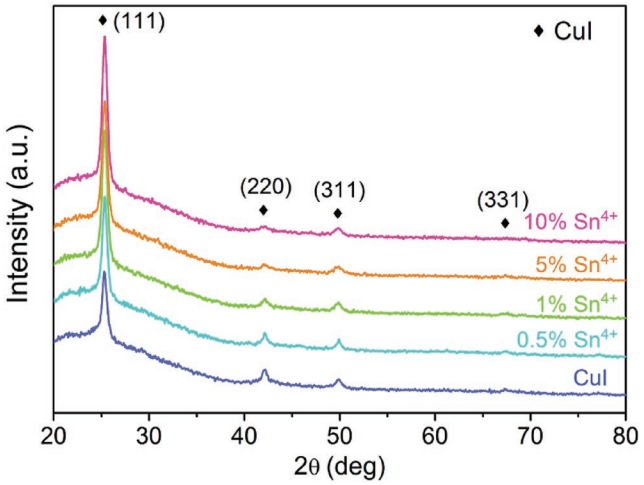

Figure 2. GIXRD patterns of CuI and Sn^{4+}-CuI samples containing 0.5%, 1%, 5%, and 10% Sn^{4+}, separately.

(311), and (331) planes of cubic CuI (JCPDS card #06-0246), and no obvious peak arising from SnI_4 phase is observed, which is consistent with the SAED results above. Furthermore there is no obvious evidence of the existence of copper oxides, to some extent indicating the stability of Sn^{4+}-CuI samples in ambient conditions. According to Figure S5a in the Supporting Information, the (111) peaks of Sn^{4+}-doped CuI samples show slight shift to the lower diffraction angle (≈0.1°) compared with that of pure CuI, which indicates that with Sn^{4+} addition the interplanar spacing of CuI increases slightly. As the ion radius of Sn^{4+} (55 pm, with coordination number of 4) is similar to that of Cu^{+} ion (60 pm, with the same coordination number of 4), the addition of Sn^{4+} may introduce interstitial defects to the tetrahedral interstitial sites of zinc-blende CuI, causing a slight expansion of the CuI lattice.[27,44] Furthermore, the average crystalline domain size along the vertical direction could be roughly estimated according to Scherrer's equation (Figure S3b, Supporting Information). Additionally, the crystal phase of hybrid Sn^{4+}-CuI/ZnO samples is also determined by the XRD method (Figure S5b, Supporting Information). The three strongest peaks of synthesized ZnO thin film centered at 31.7°, 34.4°, and 36.2° correspond to (100), (002), and (101) planes of standard ZnO. And the ZnO particle size is estimated to be ≈24.4 nm by Scherrer's equation, which is close to the particle size measured by SEM. After the deposition of Sn^{4+}-CuI on ZnO, besides the ZnO peaks mentioned above, the CuI (111) peaks become dominant in Sn^{4+}-CuI/ZnO, which is consistent with the results of Sn^{4+}-CuI.

The surface elemental composition and chemical state of the prepared Sn^{4+}-CuI on ZnO film are characterized by X-ray photoelectron spectroscopy (XPS). As is shown in Figure S6a in the Supporting Information, the existence of the elements, Cu, Sn, I, Zn, and O, is confirmed by their characteristic peaks in XPS survey spectrum. Above all, the peak centered at binding energy of 931.8 eV is corresponding to Cu 2p3/2, suggesting the Cu element exists at valence value of +1. As there is no obvious signal arising from copper (I) oxide or copper (II) oxide, it could be deduced that to some extent Sn^{4+}-CuI sample remains stable in ambient condition. Moreover, the elements Sn, I, Zn, and O are examined by XPS with their valence value of +4, −1, +2, and -2, separately. The weak peaks of element Sn indicate the low Sn content at sample surface, consistent with the small amount of Sn^{4+} addition in sample preparation. Furthermore, the existence of elements Cu, Sn, and I in 1% Sn^{4+}-CuI sample is confirmed again by X-ray energy dispersive spectrometer (EDS) study. And the homogeneous distribution of elements Cu, Sn, and I within Sn^{4+}-CuI particles is determined by the SEM mapping images in Figure S7 in the Supporting Information.

The carrier density and carrier mobility of CuI and Sn^{4+}-CuI samples are obtained by resistivity and Hall effect measurement, and the results in **Figure 3** could give us valuable insight into the electrical properties of the Sn^{4+}-CuI samples. According to Hall effect measurements, the majority carriers of the CuI and Sn^{4+}-CuI samples are proven to be holes, suggesting the samples fall into the category of p-type semiconductors. And it could be seen from Figure 3 that with the increment of Sn^{4+} addition, the carrier density increases dramatically, from 7.22×10^{16} cm^{-3} for pure CuI to 1.05×10^{19} cm^{-3} for 10% Sn^{4+}-CuI. In addition, the carrier mobility of the samples declines monotonously with Sn^{4+} addition, from 2.10 cm^2 V^{-1} s^{-1} for pure CuI to 0.06 cm^2 V^{-1} s^{-1} for 10% Sn^{4+}-CuI. Here, the cause of improved carrier density may be the introduction of massive defects to CuI by Sn^{4+} addition, and the greatly decreased carrier mobility can be ascribed to the increased probability of impurity scattering and grain boundary scattering.[12] Determined by both carrier density and

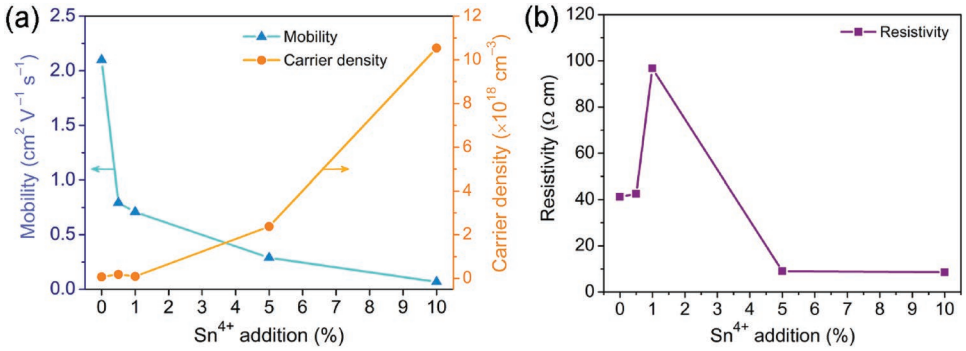

Figure 3. a) Carrier density (orange line), carrier mobility (blue line), and b) resistivity of CuI and Sn^{4+}-CuI samples with various Sn^{4+} addition by Hall effect and resistivity measurements.

© 2019 WILEY-VCH Verlag GmbH & Co. KGaA, Weinheim

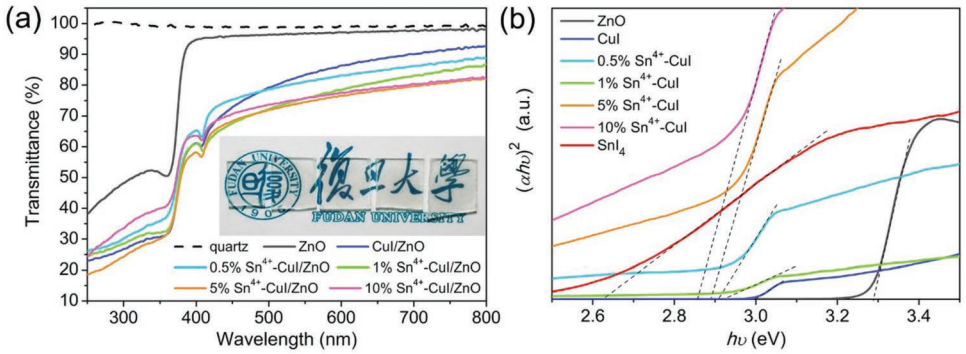

Figure 4. a) UV–vis transmission spectra of ZnO and Sn^{4+}-CuI/ZnO samples on quartz substrate. The inset picture shows the transparency of spin-coated Sn^{4+}-CuI/ZnO samples (from left to right, CuI/ZnO and Sn^{4+}-CuI/ZnO with 0.5%, 1%, 5%, and 10% Sn^{4+} addition, separately). b) Tauc plot of ZnO film, CuI, SnI_4 as well as CuI with different Sn^{4+} concentration, obtained from their absorbance spectra.

mobility, the measured resistivity of Sn^{4+}-CuI samples is shown in Figure 3b. Upon Sn^{4+} addition, the resistivity of prepared sample increases, and then decreases after reaching the peak value of 96.7 Ω cm at 1% Sn^{4+}-CuI. The obtained carrier density and mobility values herein are relatively lower than that of previously reported research on CuI thin film, and this result may arise from deteriorated contact between particles along the lateral direction as the method of Hall effect measurement requires devices with lateral structure.[12,13,45] And another possible reason for lower measured density and mobility values is the contact between semiconductor surface and the electrodes.

The optical transmittance of the Sn^{4+}-CuI/ZnO samples prepared on quartz substrate is characterized by UV–vis transmission spectroscopy. As is shown in **Figure 4**a, the ZnO film exhibits a high transparency (higher than 95%) over the visible range of 400–800 nm and a sharp absorption edge at ≈370 nm, suggesting the visible-blind and UV-responsive nature of ZnO film. After the loading of Sn^{4+}-CuI on ZnO film, the transmittance decreases in both visible light range and UV range, indicating the enhanced capability of harvesting light energy. Meanwhile, it could be observed that the Sn^{4+}-CuI/ZnO samples have visible light transmittance more than 70%, suggesting their potential for transparent electronics application. Moreover, the optical bandgap of semiconductors could be estimated by the Tauc plots based on UV–vis absorbance spectroscopy. In Figure 4b, the bandgap of ZnO nanoparticle film is estimated to be ≈3.29 eV, which corresponds to UV photon energy. For CuI and SnI_4, the bandgaps are measured to be 3.00 and 2.62 eV, respectively, while the Sn^{4+}-CuI samples exhibit bandgaps in between. And it is reasonable that with the increase of SnI_4 addition amount, the estimated bandgap narrows for Sn^{4+}-CuI samples.

The inset in **Figure 5**d shows the schematic illustration of prepared Sn^{4+}-CuI/ZnO hybrid photodetectors where two indium electrodes are fabricated on the surface of n-type ZnO and p-type Sn^{4+}-CuI separately, forming a structure of a photodiode shunted with a resistor. The current–voltage (*I–V*) curves of CuI/ZnO and Sn^{4+}-CuI/ZnO are measured under dark condition and for comparison, the *I–V* curves of pure ZnO film sample under dark and 350 nm UV light illumination are shown in Figure S8 in the Supporting Information. It could be observed that the currents of ZnO sample exhibit linear characteristic with applied bias voltage, suggesting the Ohmic contact between electrodes and ZnO film. The current at 5 V bias increases dramatically from 0.37 to 5.61 nA after its exposure to 350 nm UV illumination. In contrast to that of ZnO film detector, the dark *I–V* curves of CuI/ZnO and Sn^{4+}-CuI/ZnO samples clearly demonstrate a rectifying characteristic and dramatically decreased dark current value due to the formation of p–n junctions. Here, the exponential relationship between dark current and applied bias voltage is revealed by fitting the experimental data, which has similar form with Shockley's equation for idealized p–n junction model while with deviation to some extent.[46] And the deviation that our devices show lower current than that of idealized model at the same bias voltage, mainly arises from the resistance of ZnO film and the contacts between semiconductors and metal electrodes. And most Sn^{4+}-CuI/ZnO photodetectors show lower dark current in contrast to that of CuI/ZnO samples, implying the declined background noise of Sn^{4+}-CuI/ZnO photodetectors.

The photodetecting performance of prepared Sn^{4+}-CuI/ZnO photodetectors is characterized under UV illumination. Figure 5a compares the *I–V* curves of ZnO, CuI/ZnO, and Sn^{4+}-CuI/ZnO samples under dark and 350 nm UV light illumination. It can be noticed that with the loading of CuI or Sn^{4+}-CuI, the dark currents of the fabricated devices decline remarkably, among which the 10% Sn^{4+}-CuI/ZnO device yields the lowest dark current of 0.05 pA at bias of 5 V, which decreases by four orders of magnitude in contrast to ZnO. After 350 nm UV illumination, the photocurrents of the fabricated CuI/ZnO and Sn^{4+}-CuI/ZnO devices, except that of 1% Sn^{4+}-CuI/ZnO, show a noticeable increase compared to ZnO film. Figure 5b,c shows time-resolved photocurrent curves at 5 V bias with on/off cycling of 350 nm light illumination and their corresponding normalized photocurrent curves of the samples. Here, the time needed for current to rise till 90% of its stable maximum and to decay to 10% of its stable maximum are defined as the rise time (t_{rise}) and decay time (t_{decay}), separately. And the average characteristic parameters of prepared samples operated under 350 nm UV light at 5 V bias are summarized in **Table 1**. From *I–t* curve, the ZnO film suffers from low on/off ratio (≈5.8) and slow responsive speed (t_{rise} = 16.3 s and t_{decay} = 20.1 s) upon UV light switching resulting from surface oxygen adsorption and desorption process, which is consistent with our previous reports.[37,47] The disadvantages undoubtedly hinder the

© 2019 WILEY-VCH Verlag GmbH & Co. KGaA, Weinheim

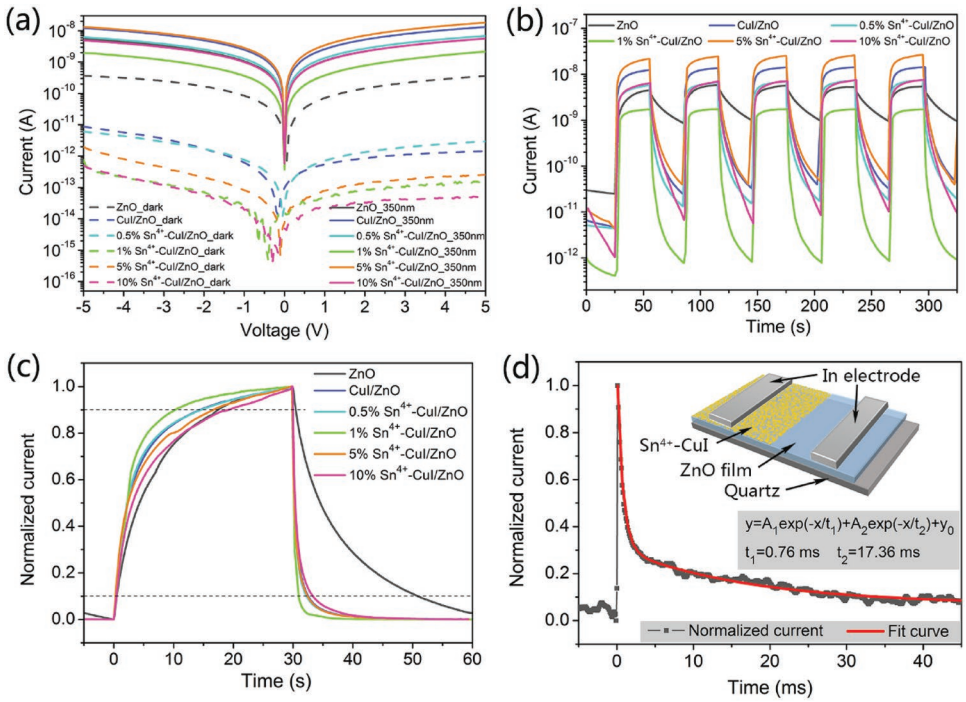

Figure 5. a) The semilogarithmic *I–V* curves for pure ZnO, CuI/ZnO, and Sn^{4+}-CuI/ZnO devices under dark (dashed lines) and 350 nm UV illumination (solid lines). b) Time-resolved photocurrent curves at 5 V bias upon 350 nm UV light switching and c) the corresponding normalized photocurrent of the samples. d) Pulse response and the exponential fit curve of the 5% Sn^{4+}-CuI/ZnO at 5 V bias. The inset shows the schematic illustration of fabricated Sn^{4+}-CuI/ZnO photodetectors.

applications of ZnO as a high-performance UV detector. And the CuI/ZnO and Sn^{4+}-CuI/ZnO samples boast dramatically increased on/off ratio upon 350 nm UV light as well as shorter response time than that of ZnO photodetector, suggesting their improved photodetecting performance after the formation of p–n junctions. Among the samples, the 5% Sn^{4+}-CuI/ZnO device exhibits the highest stable photocurrent, while the 1% Sn^{4+}-CuI/ZnO device shows the lowest stable dark current of 0.8 pA and the highest on/off ratio exceeding 2100 in response to 350 nm UV light. As for the response speed, the t_{rise} and t_{decay} of CuI/ZnO and Sn^{4+}-CuI/ZnO samples decrease when compared with that of ZnO film, with t_{decay} dropping more dramatically. Among the samples, the 1% Sn^{4+}-CuI/ZnO exhibits the shortest rise time and decay time, suggesting its fastest response speed to 350 nm UV illumination. Further, a quick response measure system with a 355 nm pulse laser source is utilized to get better insight into the time-resolved property of Sn^{4+}-CuI/ZnO sample. Here, the 5% Sn^{4+}-CuI/ZnO sample is selected for test as it exhibits the highest photocurrent in response to UV illumination and the pulse response is shown in Figure 5d. According to the result of second-order exponential fitting curve of decay current, the parameters t_1 and t_2 are calculated as 0.76 and 17.36 ms, separately, indicating the formation of heterojunction could dramatically facilitate the decay process of the photocurrent. All above results prove the fabrication of heterojunction between Sn^{4+}-CuI and ZnO to be an effective way to enhance the on/off ratio and simultaneously decrease the rise/decay time of prepared UV photodetectors based on ZnO.

The parameter of spectral responsivity of photodetectors refers to the responsivity to incident light with various wavelengths. By measuring photocurrent at certain incident wavelength, the spectral responsivity (R_λ) of photodetectors could be calculated by the following equation[48]

$$R_\lambda = (I_p - I_d)/P_\lambda S \quad (1)$$

Table 1. The summarized characteristic parameters of ZnO, CuI/ZnO, and Sn^{4+}-CuI/ZnO photodetectors under 350 nm (0.62 mW cm^{-2}) UV illumination at bias of 5 V.

Samples	Photocurrent [nA]	On/off ratio	Rise time [s]	Decay time [s]	Responsivity [mA W^{-1}]	Detectivity [× 10^9 Jones]	LDR [dB]
ZnO	5.51	5.82	16.31	20.07	0.52	4.58	16.84
CuI/ZnO	13.85	404.62	14.91	2.66	1.53	60.30	49.79
0.5% Sn^{4+}-CuI/ZnO	6.94	402.97	14.74	2.45	1.18	65.20	51.10
1% Sn^{4+}-CuI/ZnO	1.72	2102.49	10.41	1.08	0.44	135.76	69.38
5% Sn^{4+}-CuI/ZnO	25.04	544.50	19.61	2.65	2.62	323.15	74.27
10% Sn^{4+}-CuI/ZnO	7.20	917.92	18.18	3.39	0.59	33.83	50.82

© 2019 WILEY-VCH Verlag GmbH & Co. KGaA, Weinheim

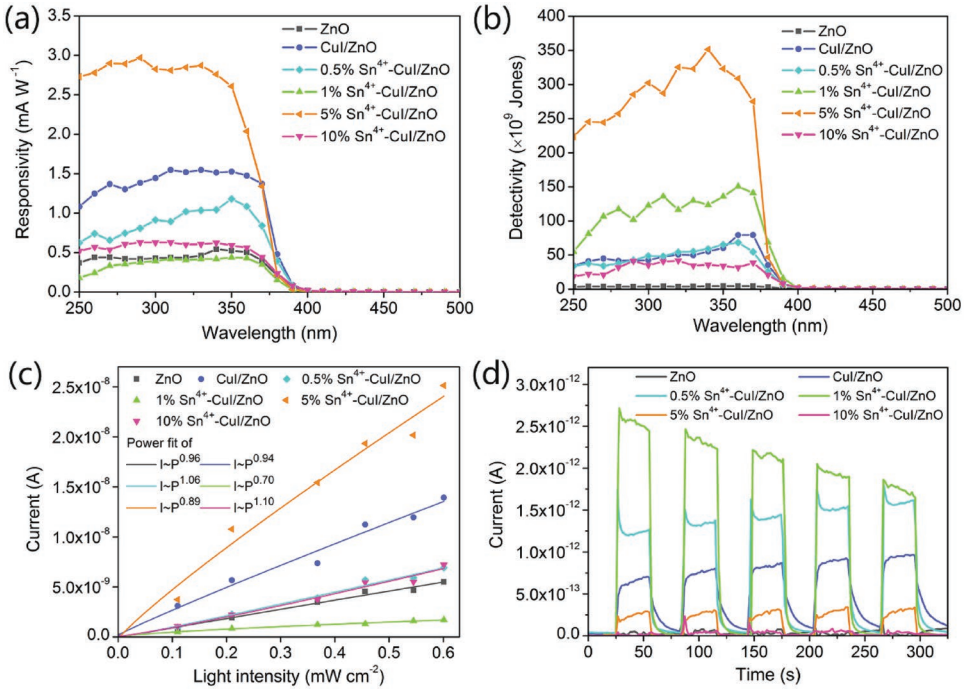

Figure 6. The spectral a) responsivity and b) detectivity of the prepared samples at 5 V bias, respectively. c) The variation of the stable photocurrent as a function of incident power density (350 nm UV light) at 5 V bias. d) *I–t* curves under 350 nm UV light switching at 0 V bias.

where I_p and I_d refer to photocurrent and dark current, P_λ is the incident power density, and S is the effective exposure area. The measured spectral responsivity of the fabricated devices at bias of 5 V is shown in **Figure 6**a. A sharp cutoff wavelength could be observed for all the devices at the wavelength of ≈390 nm, demonstrating their potential as visible-blind UV detectors. According to the results, for pure ZnO thin film, its highest responsivity (0.53 mA W^{-1}) locates at ≈350 nm, which is consistent with the bandgap value of ZnO measured by UV–vis spectroscopy (Figure 4a). Among the hybrid photodetectors, the 5% Sn^{4+}-CuI/ZnO sample shows the highest responsivity at UV range, followed by CuI/ZnO, 0.5% Sn^{4+}-CuI/ZnO, 10% Sn^{4+}-CuI/ZnO, and 1% Sn^{4+}-CuI/ZnO samples. In addition, the UV-to-visible rejection ratio, which refers to the detective sensitivity of detectors in UV range compared to that of visible light range, is defined herein as $R_{350\ nm}/R_{500\ nm}$. All the fabricated hybrid detectors are observed to have a rejection ratio higher than 1000, with 1% Sn^{4+}-CuI/ZnO showing the highest rejection ratio of ≈5010, suggesting their potential as visible-blind photodetectors. Additionally, the parameter of detectivity, or the capability of signal detection from noise environment, is another crucial parameter for photodetectors. Generally, the detectivity (D^*) can be calculated as following when taking dark current into consideration[49,50]

$$D^* = R_\lambda \left(2qI_d/S\right)^{-1/2} \quad (2)$$

where q is elementary charge. As is shown in Figure 6b, the detectivity of Sn^{4+}-CuI/ZnO sample increases with the increment of Sn^{4+} addition and then begins to decline after the 5% Sn^{4+}-CuI/ZnO sample reaches the highest detectivity of 3.5×10^{11} Jones at wavelength of 340 nm, which is 153 times the value of ZnO and 4.6 times the value of CuI/ZnO. And the result indicates the Sn^{4+}-CuI/ZnO devices have the capability to detect UV signal more effectively and an optimal amount of Sn^{4+} doping is needed toward optimized performance.

Besides, the dependence between photocurrent and the power density is revealed by adjusting the incident power density. Figure 6c shows the photocurrents of prepared samples under various incident power density of 350 nm at 5 V bias. It can be seen that all the photocurrents are obviously enhanced with the increase of incident light power density, and the experimental results could be fitted by power-law equations, $I_p \sim P^a$.[51,52] For the most of the samples, the value of a is relatively close to 1, suggesting their near-linear photocurrent–intensity dependence. According to previous study, the power-law relationship between photocurrent and incident power density is related to the existence of surface carrier traps, and low concentration of surface traps will lead to near-linear photocurrent–intensity dependence.[53–55] Moreover, the *I–t* curves of the fabricated devices under illumination of 350 nm UV light at 0 V bias are shown in Figure 6d, from which the highest photocurrent of ≈2.5 pA and the highest on/off ratio of ≈320 are observed in 1% Sn^{4+}-CuI/ZnO sample under 350 nm UV light switching, outperforming ZnO metal-semiconductor-metal (MSM) photodetector and CuI/ZnO sample (with on/off ratio of ≈12), thanks to their greatly decreased dark current and built-in electric field. The results suggest Sn^{4+}-CuI/ZnO photodetectors have the capability of operating without external power supply, revealing the potential of Sn^{4+}-CuI/ZnO samples as self-powered photodetectors.

As is shown in Figure 4a, the transmittance of the samples decreases obviously after the loading of CuI or Sn^{4+}-CuI on ZnO; therefore, it is possible for CuI or Sn^{4+}-CuI to block incident UV light and lead to lower photoresponsivity of the hybrid

© 2019 WILEY-VCH Verlag GmbH & Co. KGaA, Weinheim

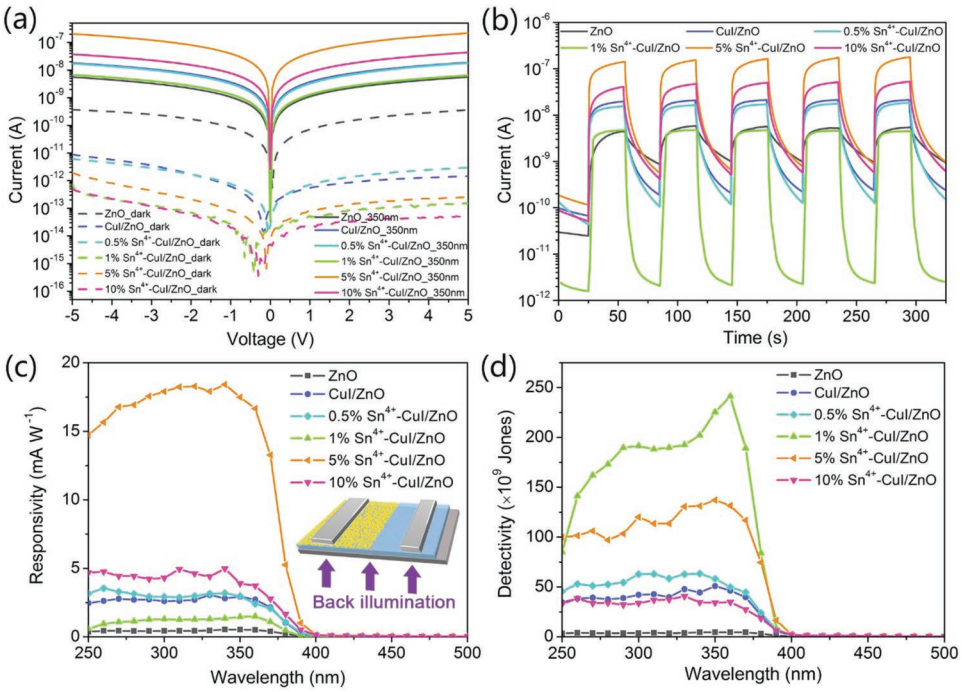

Figure 7. a) The semilogarithmic *I–V* curves for pure ZnO, CuI/ZnO, and Sn^{4+}-CuI/ZnO devices under dark (dashed lines) and 350 nm backside UV illumination (solid lines). b) Time-resolved photocurrent curves at 5 V bias upon 350 nm UV light switching from backside. The spectral c) responsivity and d) detectivity of the prepared samples under backside UV illumination at 5 V bias, respectively.

photodetectors. As a result, further experiments are carried out to investigate the photodetecting performances of the fabricated devices when illuminated from their backside (the schematic illustration shown in the inset of **Figure 7**c). Figure 7a,b and **Table 2** show that under backside UV illumination, the hybrid photodetectors exhibit improved photocurrent than that of samples illuminated from front side. It is reasonable for the hybrid photodetectors to yield higher photocurrent under backside illumination as CuI or Sn^{4+}-CuI shows lower optical transmittance than that of ZnO film and the shading effect arising from the loading of CuI or Sn^{4+}-CuI could be eliminated under backside UV illumination. And from *I–t* curves, the 5% Sn^{4+}-CuI/ZnO sample boast the highest photocurrent of 162.71 nA during 30 s backside UV light switching, which is 6.5 times the value when illuminated from front side and 7.8 times the value of back-illuminated CuI/ZnO. As a result the responsivity of back-illuminated hybrid photodetectors is improved significantly (Figure 7c), among which the 5% Sn^{4+}-CuI/ZnO sample has the highest responsivity of 17.49 mA W^{-1} at the wavelength of 350 nm, which is 6.6 times the value when being front-illuminated. It is interesting to notice that except the 10% Sn^{4+}-CuI, the Sn^{4+}-CuI samples with lower resistivity (Figure 3) yield higher photocurrent in Sn^{4+}-CuI/ZnO, suggesting the important role the resistivity of Sn^{4+}-CuI plays on the photocurrent of hybrid photodetectors. In addition, the average rise time (t_{rise}) of photocurrent decreases and average decay time (t_{decay}) increases when illuminated from backside, and among those back-illuminated the 1% Sn^{4+}-CuI/ZnO shows the fastest response speed. The shortened t_{rise} and improved t_{decay} may be a consequence of declined shading effect and prolonged recombination process for the increased number of photoinduced electron–hole pairs. Therefore, there is, simultaneously, an increase in dark current value of backside-illuminated samples because in the decay process the photocurrent could barely fall to the same level as front-illuminated samples within the same duration, which leads to the lower on/off ratio and detectivity of

Table 2. The summarized characteristic parameters of ZnO, CuI/ZnO, and Sn^{4+}-CuI/ZnO photodetectors under 350 nm (0.62 mW cm^{-2}) UV illumination from backside at bias of 5 V.

Samples	Photocurrent [nA]	On/off ratio	Rise time [s]	Decay time [s]	Responsivity [mA W^{-1}]	Detectivity [× 10^9 Jones]	LDR [dB]
ZnO	5.50	5.61	16.49	19.29	0.51	4.57	16.82
CuI/ZnO	20.87	94.51	12.62	4.52	2.93	50.87	39.77
0.5% Sn^{4+}-CuI/ZnO	17.08	136.29	12.08	4.82	2.98	58.26	41.98
1% Sn^{4+}-CuI/ZnO	4.62	2012.59	8.25	1.11	1.46	225.33	66.34
5% Sn^{4+}-CuI/ZnO	162.71	212.79	19.58	3.02	17.49	137.16	43.99
10% Sn^{4+}-CuI/ZnO	48.48	89.93	17.51	5.19	3.90	34.16	31.96

© 2019 WILEY-VCH Verlag GmbH & Co. KGaA, Weinheim

back-illuminated samples. As for detectivity, the 1% Sn^{4+}-CuI/ZnO exhibits the highest detectivity, thanks to the lowest dark current it reaches. Consequently, the photocurrent and responsivity could be further improved for the hybrid photodetectors when back-illuminated.

The photoluminescence (PL) spectra and Gaussian-fitted PL spectra of ZnO, CuI/ZnO, and Sn^{4+}-CuI/ZnO samples with excitation wavelength of 320 nm are shown in Figure S9 in the Supporting Information. The strongest UV emission peak centered at ≈390 nm is related to the direct recombination of photogenerated electron–hole pairs of ZnO, according to previous reports.[56] It could be seen that with Sn^{4+}-CuI loading the intensity of PL peaks centered at ≈390 nm decreases greatly, consequently the formation of p–n junction between ZnO and Sn^{4+}-CuI would effectively reduce the recombination probability and lead to improved photodetecting performance as discussed above. In Gaussian-fitted PL spectrum of ZnO film, the PL peak at 387 nm is fitted into two bands centered at 378 and 390 nm, separately. Those two bands, along with the band centered at ≈360 nm, are possibly related to the exciton emission process of ZnO and oxygen vacancies.[47,57] As for Sn^{4+}-CuI/ZnO samples, the emission peaks centered at ≈420 nm emerge and this band may be associated with the CuI emission arising from Cu^{+} vacancies in the crystal lattice.[58,59] On the issue of photoluminescent properties, further research is still needed to investigate the luminescence mechanism of CuI after Sn^{4+} doping.

The schematic illustration and the equivalent circuit of prepared Sn^{4+}-CuI/ZnO photodetectors are shown in **Figure 8**a. The structure of the photodetectors is described as a photodiode shunted with a resistor, where the interface between Sn^{4+}-CuI and ZnO is equivalent to a diode and the In-ZnO contact is depicted as a shunt resister. The current–voltage curves of CuI/ZnO and Sn^{4+}-CuI/ZnO under dark condition (Figure S8, Supporting Information) discussed above exhibit rectification characteristic, suggesting the validity of the equivalent circuit. Depending on the results discussed above, there are three main causes that account for the enhanced performance of Sn^{4+}-CuI/ZnO when compared with ZnO as well as CuI/ZnO photodetectors, and the performance variation of Sn^{4+}-CuI/ZnO samples with different Sn^{4+} addition. Above all, the formation of p–n junctions between p-type Sn^{4+}-CuI and n-type ZnO would greatly improve the photodetection performance. As is shown in Figure 4b, the optical bandgaps of n-type ZnO and p-type Sn^{4+}-CuI are measured as 3.29 and 2.85–3.00 eV, separately, by UV–vis spectroscopy. And it is deduced from the valence band (VB) XPS spectrum of 1% Sn^{4+}-CuI sample shown in Figure S10 in the Supporting Information that the position of valence band is 0.32 eV lower relative to its Fermi level and the valence band position of ZnO is determined in previous report under the same preparation condition.[37] Therefore, a typical type-II heterojunction is formed between p-type Sn^{4+}-CuI and n-type ZnO in the hybrid photodetectors (Figure 8b). The built-in electric field at depletion layer will endow the hybrid photodetectors with dramatically decreased dark current under reverse bias in contrast to ZnO MSM detectors. And it is widely accepted that a type-II p–n junction could effectively facilitate the separation process of photogenerated electron–hole pairs due to the effect of built-in electric field.[3,60] Under UV illumination, the photogenerated minority carriers in p-type Sn^{4+}-CuI (electrons) would transport effectively to n-type ZnO, leading to enhanced photocurrents of Sn^{4+}-CuI/ZnO devices, and vice versa.[37] And the response time could also be declined by suppressing oxygen desorption and readsorption process at ZnO surface due to enhanced charge separation efficiency.[47] Moreover, with the photoinduced electron–hole pairs being separated by built-in electric field, the photovoltaic effect of p–n junctions could provide the hybrid photodetectors with possibility to operate under 0 V bias (Figure 6d).

By varying the Sn^{4+} concentration, the morphology and resistivity of Sn^{4+}-CuI could be successfully manipulated, which have substantial effect on the photodetecting performance of Sn^{4+}-CuI/ZnO detectors. The carrier density and mobility of p-type Sn^{4+}-CuI could be tuned by adjusting the Sn^{4+} addition. As discussed above, with the shading effect of CuI or Sn^{4+}-CuI eliminated, it could be concluded from the back-illuminated samples that the Sn^{4+}-CuI samples with lower resistivity yield higher photocurrent in the corresponding Sn^{4+}-CuI/ZnO detectors. For instance, the 5% Sn^{4+}-CuI/ZnO shows the highest photocurrent as well as responsivity due to its relatively low resistivity among the Sn^{4+}-CuI samples. Moreover, the Sn^{4+} addition in CuI, as is shown in SEM and AFM results, has significant effect on the morphology of prepared Sn^{4+}-CuI particles. With the evaporation of solvent, the CuI nanoparticles come into existence on the substrate during spin-coating procedure. The CuI/ZnO device shows improved photocurrent and shortened response time than that of pure ZnO, but the CuI/ZnO interface is insufficient to separate photoinduced carrier pairs effectively due to the poor contact formed between stacked CuI particles and ZnO, as is shown in Figure 8c. And the formation of Sn^{4+}-CuI thin sheets with large lateral scale is observed when Sn^{4+} addition is relatively low. As

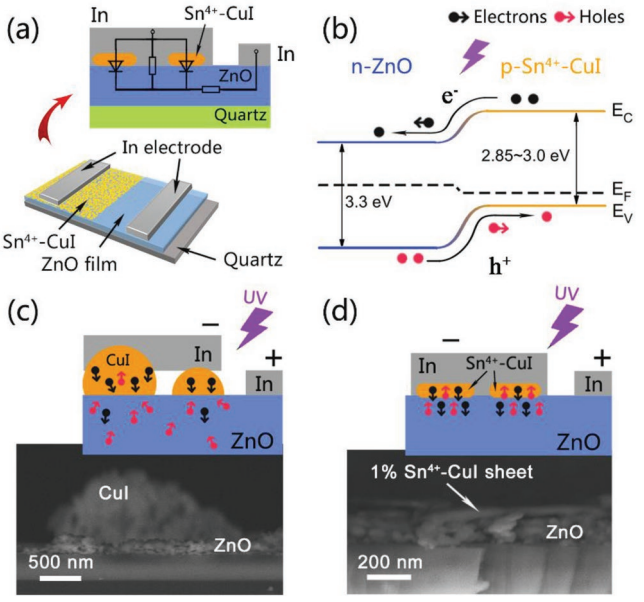

Figure 8. Proposed mechanism of p-Sn^{4+}-CuI/n-ZnO photodetectors. a) Schematic illustration and the equivalent circuit of Sn^{4+}-CuI/ZnO hybrid photodetectors. b) The band alignment of Sn^{4+}-CuI/ZnO hybrid photodetectors under UV illumination. c) The cross-sectional SEM image and proposed mechanism of CuI/ZnO. d) The cross-sectional SEM image showing 1% Sn^{4+}-CuI sheet on ZnO film and proposed mechanism for enhanced photodetecting performance of Sn^{4+}-CuI/ZnO.

© 2019 WILEY-VCH Verlag GmbH & Co. KGaA, Weinheim

for photodetecting performance, the 1% Sn^{4+}-CuI/ZnO device shows the lowest dark current, highest on/off ratio and detectivity among those fabricated devices, and the enhanced performance is inextricably linked with the optimized morphology and interface contact. As is shown in Figure 8d, with the large thin sheets lying on the upper surface of ZnO, the large-area contact of high quality between Sn^{4+}-CuI and ZnO would greatly facilitate the separation and transport of photoinduced carriers. However, as shown in Figure 1f and Figure S2e in the Supporting Information, an even higher Sn^{4+} concentration (10%) would cause lattice distortion in 10% Sn^{4+}-CuI, resulting in the deteriorated interface contact. The poor contact would undoubtedly lead to inferior photodetecting performance of 10% Sn^{4+}-CuI/ZnO, such as low on/off ratio, slow response speed, and declined detectivity compared with other Sn^{4+}-CuI/ZnO devices, despite the low resistivity of 10% Sn^{4+}-CuI (Figure 3b). In general, by varying Sn^{4+} addition, the morphology, bandgap as well as electrical transport properties of Sn^{4+}-CuI could be successfully and easily controlled, which provides possibility for fabricating UV photodetectors of enhanced performance.

3. Conclusion

In summary, Sn^{4+}-doped CuI is successfully prepared via facile solution process and is characterized by multiple characterization methods. And for the first time, the potential of Sn^{4+}-CuI as a p-type component toward high performance UV photodetection is investigated by constructing transparent Sn^{4+}-CuI/ZnO hybrid photodetectors. The doping of Sn^{4+} shows great effect on the micromorphology as the formation of Sn^{4+}-CuI thin sheets is observed, while the effect on the lattice constants of CuI is limited as Sn^{4+} shares similar ion radius with Cu^{+}. It is found that Sn^{4+}-CuI/ZnO hybrid photodetectors exhibit obviously improved photodetecting performance outperforming ZnO film as well as CuI/ZnO photodetectors under the same preparation method, including significantly improved on/off ratio, responsivity, and shortened response time upon UV light switching. The hybrid photodetectors show even higher photocurrent and responsivity when illuminated from backside, with the shading effect of Sn^{4+}-CuI eliminated. The enhanced photodetecting performance of Sn^{4+}-CuI/ZnO hybrid photodetectors is attributed to the formation of type-II p-Sn^{4+}-CuI/n-ZnO heterojunctions. The built-in electric field facilitates the separation of photoinduced electron–hole pairs under UV illumination and suppresses oxygen desorption/adsorption at ZnO surface, resulting in higher photocurrent and shortened response time. And the existence of ultrathin Sn^{4+}-CuI sheets provides better contact and higher carrier separation efficiency via Sn^{4+} addition, leading to improved photodetecting performance of Sn^{4+}-CuI/ZnO than that of CuI/ZnO. However, an excess of Sn^{4+} addition would cause lattice distortion in Sn^{4+}-CuI and poor interface contact, leading to inferior photodetecting performance. Furthermore, by adjusting Sn^{4+} concentration, the electrical resistivity of Sn^{4+}-CuI could be tuned because of the increased carrier density and the simultaneously decreased mobility, which also has a significant effect on the photocurrent of Sn^{4+}-CuI/ZnO detectors. This study provides insight into the unique properties of Sn^{4+}-doped CuI and opens opportunities for the exploitation of CuI for various applications beyond.

4. Experimental Section

Synthesis of ZnO Film: The ZnO film was prepared by sol–gel method as previously reported.[47] Briefly, 1.44 g of $Zn(CH_3COO)_2{\cdot}2H_2O$ (>99%) was dissolved in the mixture of 1 mL ethanol and 9 mL deionized water, and 0.75 g of poly(vinyl alcohol) (PVA-1788 low-viscosity, MW ≈44.05, Aladdin) was added under vigorous stirring. Then, 0.5 mL of CH_3COOH was added dropwise into the solution after PVA-1788 was totally dissolved, and the solution was kept for an aging time of 24 h before the spin-coating process. Quartz and silicon substrates were cleaned thoroughly with acetone, ethanol, and deionized water by sonication, and then treated by plasma (air) cleaning method. The precursor was then spin-coated on cleaned substrates at a spin speed of 500 rpm for 6 s and 3000 rpm for another 20 s, dried at 60 °C for 10 min, and then annealed at 450 °C for 2 h.

Fabrication of Sn^{4+}-CuI/ZnO: Copper (I) iodide (CuI, >99.5%, Aladdin) and tin (IV) iodide (SnI_4, >95%, Alfa Aesar) were dissolved in acetonitrile (>99.5%, Aladdin) by sonication. Then, 2-methoxyethanol was added into the solution with the volume ratio of acetonitrile/2-methoxyethanol of 3:1. The addition of 2-methoxyethanol could improve the viscosity and decrease the evaporation rate of acetonitrile solution, thus leading to improved spin-coating quality. The total concentration of metal elements was kept at 0.1 M. After that, Sn^{4+}-CuI solution was spin-coated on annealed ZnO film to fabricate Sn^{4+}-CuI/ZnO sample at a spin speed of 500 rpm for 6 s and 2500 rpm for another 30 s. And Sn^{4+}-CuI samples with Sn^{4+} addition of 0.5%, 1%, 5%, and 10% were denoted as 0.5% Sn^{4+}-CuI, 1% Sn^{4+}-CuI, 5% Sn^{4+}-CuI, and 10% Sn^{4+}-CuI, separately.

Characterization of Sn^{4+}-CuI/ZnO Film: The morphology and element composition of the Sn^{4+}-CuI/ZnO film was investigated by field-emission scanning electron microscopy (Zeiss Sigma) and X-ray EDS. Selective area electron diffraction of the Sn^{4+}-CuI samples was conducted on TEM (FEI Tecnai F30). The AFM measurement was conducted on a Bruker Dimension Edge atomic force microscopy. The grazing incidence X-ray diffraction measurement was conducted on a Rigaku Smartlab9 diffractometer to observe the crystal structures of Sn^{4+}-CuI samples using Cu Kα radiation (λ = 1.5406 Å) at a scan rate of 10° min^{-1}. The surface elemental composition and chemical state of the Sn^{4+}-CuI/ZnO samples were measured by X-ray photoelectron spectroscopy using a PHI 5300 ESCA system (Mg, 14 kV, 250 W). UV–vis transmission and absorption spectroscopy was obtained using a UV–vis spectrophotometer (Hitachi U-3900H). Hall effect measurements were performed on a four-probe MMR H50 system. Photoluminescence emission spectra were obtained on Varian Cary Eclipse spectrofluorometer with excitation wavelength of 320 nm.

Photoelectronic Measurements: Indium was used as electrodes for the fabrication of Sn^{4+}-CuI/ZnO photodetectors. And the photodetecting performance of Sn^{4+}-CuI/ZnO was characterized using a semiconductor characterization system (Keithley 4200, USA). The light source was a 450 W Xenon lamp equipped with a monochromator, whose light flux intensity was measured with a NOVA II power meter (OPHIR Photonics). The pulse response of the sample was tested by a digital oscilloscope (Tektronix DPO 5140B) and a 355 nm Nd:YAG pulsed laser system with pulse duration of 3–5 ns.

Supporting Information

Supporting Information is available from the Wiley Online Library or from the author.

Acknowledgements

The authors appreciate Dr. Weixin Ouyang, Dr. Zhiming Zhang, Yajie Yan, and Hong Zhu for their kind support to this work. This work was supported by the National Key Research and Development Program of China (Grant No. 2017YFA0204600), the National Natural Science Foundation of China (NSFC Grant Nos. 51721002, 51872050, 11674061, and 11811530065), the Science and Technology Commission of Shanghai Municipality (Grant Nos. 18520744600, 18520710800, and

 © 2019 WILEY-VCH Verlag GmbH & Co. KGaA, Weinheim

17520742400), the Ministry of Education Joint Fund for Equipment Pre-Research (6141A02033241), and the Open Project of the State Key Laboratory of Luminescence and Applications (SKLA-2018-05). Part of the research was carried out in Fudan Nanofabrication Laboratory.

Conflict of Interest

The authors declare no conflict of interest.

Keywords

doped CuI, photodetectors, solution process, transparent, ZnO

Received: April 15, 2019
Published online: May 20, 2019

[1] E. Monroy, F. Omnès, F. Calle, *Semicond. Sci. Technol.* **2003**, *18*, R33.
[2] X. Xu, J. Chen, S. Cai, Z. Long, Y. Zhang, L. Su, S. He, C. Tang, P. Liu, H. Peng, X. S. Fang, *Adv. Mater.* **2018**, *30*, 1803165.
[3] X. Liu, L. Gu, Q. Zhang, J. Wu, Y. Long, Z. Fan, *Nat. Commun.* **2014**, *5*, 4007.
[4] Y. Ning, Z. M. Zhang, F. Teng, X. S. Fang, *Small* **2018**, *14*, 1703754.
[5] S. F. Leung, K. T. Ho, P. K. Kung, V. K. S. Hsiao, H. N. Alshareef, Z. L. Wang, J. H. He, *Adv. Mater.* **2018**, *30*, 1704611.
[6] Y. Zhang, W. Xu, X. Xu, J. Cai, W. Yang, X. S. Fang, *J. Phys. Chem. Lett.* **2019**, *10*, 836.
[7] B. Zhao, F. Wang, H. Chen, L. Zheng, L. Su, D. Zhao, X. S. Fang, *Adv. Funct. Mater.* **2017**, *27*, 1700264.
[8] C. Li, C. Han, Y. Zhang, Z. Zang, M. Wang, X. Tang, J. Du, *Sol. Energy Mater. Sol. Cells* **2017**, *172*, 341.
[9] J. Cai, X. Xu, L. Su, W. Yang, H. Chen, Y. Zhang, X. S. Fang, *Adv. Opt. Mater.* **2018**, *6*, 1800213.
[10] K. Nomura, H. Ohta, A. Takagi, T. Kamiya, M. Hirano, H. Hosono, *Nature* **2004**, *432*, 488.
[11] F. Teng, K. Hu, W. X. Ouyang, X. S. Fang, *Adv. Mater.* **2018**, *30*, 1706262.
[12] T. Jun, J. Kim, M. Sasase, H. Hosono, *Adv. Mater.* **2018**, *30*, 1706573.
[13] M. Grundmann, F.-L. Schein, M. Lorenz, T. Böntgen, J. Lenzner, H. von Wenckstern, *Phys. Status Solidi A* **2013**, *210*, 1671.
[14] J. A. Christians, R. C. M. Fung, P. V. Kamat, *J. Am. Chem. Soc.* **2014**, *136*, 758.
[15] H.-Q. Do, O. Daugulis, *J. Am. Chem. Soc.* **2008**, *130*, 1128.
[16] C. Yang, D. Souchay, M. Kneiß, M. Bogner, H. M. Wei, M. Lorenz, O. Oeckler, G. Benstetter, Y. Q. Fu, M. Grundmann, *Nat. Commun.* **2017**, *8*, 16076.
[17] C. Gao, X. Zhu, L. Zhang, D. Zhou, Z. Wang, L. Liao, *Appl. Phys. Lett.* **2013**, *102*, 153301.
[18] G. A. Sepalage, S. Meyer, A. Pascoe, A. D. Scully, F. Huang, U. Bach, Y.-B. Cheng, L. Spiccia, *Adv. Funct. Mater.* **2015**, *25*, 5650.
[19] M. Li, Z. Wang, Y. Yang, Y. Hu, S. Feng, J. Wang, X. Gao, L. Liao, *Adv. Energy Mater.* **2016**, *6*, 1601156.
[20] J. Chen, N.-G. Park, *J. Phys. Chem. C* **2018**, *122*, 14039.
[21] H. Kang, R. Liu, K. Chen, Y. Zheng, Z. Xu, *Electrochim. Acta* **2010**, *55*, 8121.
[22] N. Yamada, R. Ino, Y. Ninomiya, *Chem. Mater.* **2016**, *28*, 4971.
[23] C. Yang, M. Kneiß, F.-L. Schein, M. Lorenz, M. Grundmann, *Sci. Rep.* **2016**, *6*, 21937.
[24] W. Sun, H. Peng, Y. Li, W. Yan, Z. Liu, Z. Bian, C. Huang, *J. Phys. Chem. C* **2014**, *118*, 16806.
[25] J. Wang, J. Li, S. Li, *J. Appl. Phys.* **2011**, *110*, 054907.
[26] J. Zhu, M. Gu, R. Pandey, *J. Phys. Chem. Solids* **2013**, *74*, 1122.
[27] M. Xia, M. Gu, X. Liu, B. Liu, S. Huang, C. Ni, *J. Mater. Sci.: Mater. Electron.* **2015**, *26*, 2629.
[28] S. Yue, M. Gu, X. Liu, F. Li, S. Liu, X. Zhang, J. Zhang, B. Liu, S. Huang, C. Ni, *Mater. Res. Bull.* **2018**, *106*, 228.
[29] L. A. DeSilva, J. Harwell, A. Gaquere-Parker, U. A. G. Perera, K. Tennakone, *Phys. Status Solidi A* **2017**, *214*, 1700520.
[30] K. Sun, Y. Jing, N. Park, C. Li, Y. Bando, D. Wang, *J. Am. Chem. Soc.* **2010**, *132*, 15465.
[31] Q. Liu, M. Gong, B. Cook, D. Ewing, M. Casper, A. Stramel, J. Wu, *J. Mater. Chem. C* **2017**, *5*, 6427.
[32] K. Liu, M. Sakurai, M. Liao, M. Aono, *J. Phys. Chem. C* **2010**, *114*, 19835.
[33] K. Zhang, Y. Yang, *Adv. Funct. Mater.* **2017**, *27*, 1703331.
[34] C. Soci, A. Zhang, B. Xiang, S. A. Dayeh, D. P. R. Aplin, J. Park, X. Y. Bao, Y. H. Lo, D. Wang, *Nano Lett.* **2007**, *7*, 1003.
[35] S. M. Hatch, J. Briscoe, S. Dunn, *Adv. Mater.* **2013**, *25*, 867.
[36] C.-L. Hsu, Y.-D. Gao, Y.-S. Chen, T.-J. Hsueh, *ACS Appl. Mater. Interfaces* **2014**, *6*, 4277.
[37] W. Ouyang, F. Teng, M. Jiang, X. S. Fang, *Small* **2017**, *13*, 1702177.
[38] L. Su, H. Chen, X. Xu, X. S. Fang, *Laser Photonics Rev.* **2017**, *11*, 1700222.
[39] Y. Zhang, S. Y. Li, W. Yang, M. K. Joshi, X. S. Fang, *J. Phys. Chem. Lett.* **2019**, *10*, 2400.
[40] F.-L. Schein, H. von Wenckstern, M. Grundmann, *Appl. Phys. Lett.* **2013**, *102*, 092109.
[41] N. Yamada, Y. Kondo, X. Cao, Y. Nakano, *Appl. Mater. Today* **2019**, *15*, 153.
[42] Z. Yang, M. Wang, J. Ding, Z. Sun, L. Li, J. Huang, J. Liu, J. Shao, *ACS Appl. Mater. Interfaces* **2015**, *7*, 21235.
[43] J. Liu, Y. Zhang, C. Liu, M. Peng, A. Yu, J. Kou, W. Liu, J. Zhai, J. Liu, *Nanoscale Res. Lett.* **2016**, *11*, 281.
[44] R. D. Shannon, *Acta Crystallogr., Sect. A: Found. Adv.* **1976**, *32*, 751.
[45] S. Inudo, M. Miyake, T. Hirato, *Phys. Status Solidi A* **2013**, *210*, 2395.
[46] W. Shockley, *Bell Syst. Tech. J.* **1949**, *28*, 435.
[47] F. Teng, W. Ouyang, Y. Li, L. Zheng, X. S. Fang, *Small* **2017**, *13*, 1700156.
[48] W. Yang, K. Hu, F. Teng, J. Weng, Y. Zhang, X. S. Fang, *Nano Lett.* **2018**, *18*, 4697.
[49] L. Shen, Y. Fang, H. Wei, Y. Yuan, J. Huang, *Adv. Mater.* **2016**, *28*, 2043.
[50] H. Chen, P. Yu, Z. Zhang, F. Teng, L. Zheng, K. Hu, X. S. Fang, *Small* **2016**, *12*, 5809.
[51] D. Wu, Y. Jiang, Y. Zhang, J. Li, Y. Yu, Y. Zhang, Z. Zhu, L. Wang, C. Wu, L. Luo, J. Jie, *J. Mater. Chem.* **2012**, *22*, 6206.
[52] L. X. Zheng, K. Hu, F. Teng, X. S. Fang, *Small* **2017**, *13*, 1602448.
[53] Y. L. Cao, Z. T. Liu, L. M. Chen, Y. B. Tang, L. B. Luo, J. S. Jie, W. J. Zhang, S. T. Lee, C. S. Lee, *Opt. Express* **2011**, *19*, 6100.
[54] S.-C. Kung, W. Xing, W. E. van der Veer, F. Yang, K. C. Donavan, M. Cheng, J. C. Hemminger, R. M. Penner, *ACS Nano* **2011**, *5*, 7627.
[55] C. J. Liu, S. Chen, J. Li, *J. Inorg. Mater.* **2018**, *33*, 1343.
[56] X. L. Wu, G. G. Siu, C. L. Fu, H. C. Ong, *Appl. Phys. Lett.* **2001**, *78*, 2285.
[57] Z. Fang, Y. Wang, D. Xu, Y. Tan, X. Liu, *Opt. Mater.* **2004**, *26*, 239.
[58] D. Chen, Y. Wang, Z. Lin, J. Huang, X. Chen, D. Pan, F. Huang, *Cryst. Growth Des.* **2010**, *10*, 2057.
[59] G. Lin, F. Zhao, Y. Zhao, D. Zhang, L. Yang, X. Xue, X. Wang, C. Qu, Q. Li, L. Zhang, *Materials* **2016**, *9*, 990.
[60] W. X. Ouyang, F. Teng, X. S. Fang, *Adv. Funct. Mater.* **2018**, *28*, 1707178.

 © 2019 WILEY-VCH Verlag GmbH & Co. KGaA, Weinheim